

## Article

# Effects of the Operating Parameters of Supersonic Separators on the Supersonic Liquefaction Characteristics of Natural Gas

Xueyuan Long, Qian Huang \*, Yuan Tian and Lingyan Mu

School of Petroleum Engineering, Chongqing University of Science and Technology, Chongqing 401331, China; 2007078@cqust.edu.cn (X.L.); swpu\_tianyuan@126.com (Y.T.); mulingyan323@163.com (L.M.)

\* Correspondence: huangqianswpu@163.com

**Abstract:** In this study, a mathematical model for the supersonic condensate flow of natural gas to understand its condensation process in a supersonic separator has been proposed. The effects of export back pressure, inlet temperature, and inlet pressure on the condensation parameters were investigated. The results indicate that the condensation position moves forward with the increase in the inlet pressure and the decrease in the inlet temperature. A method for determining the optimal range of operating parameters (export back pressure, inlet temperature, and inlet pressure) for the supersonic separator is proposed. Within the optimal back pressure range, the region of extreme Mach number in the device should be at the inlet of the straight pipe section after the separation gap, and extreme value distribution areas of low temperature, condensation nucleation, and humidity should be between the nozzle expansion section and the inlet of the straight pipe section. It is important to choose a higher temperature among the optimal values as the inlet temperature and also ensure that the optimal inlet pressure is not higher than the pressure corresponding to the humidity inflection point. At the optimal inlet pressure, the maximum humidity distribution area should be behind the supersonic nozzle expansion section and in front of the inlet of the straight pipe section.

**Keywords:** natural gas; liquefaction; condensation; supersonic separator



**Citation:** Long, X.; Huang, Q.; Tian, Y.; Mu, L. Effects of the Operating Parameters of Supersonic Separators on the Supersonic Liquefaction Characteristics of Natural Gas. *Energies* **2022**, *15*, 2531. <https://doi.org/10.3390/en15072531>

Academic Editor: Phillip Ligrani

Received: 25 January 2022

Accepted: 28 March 2022

Published: 30 March 2022

**Publisher's Note:** MDPI stays neutral with regard to jurisdictional claims in published maps and institutional affiliations.



**Copyright:** © 2022 by the authors. Licensee MDPI, Basel, Switzerland. This article is an open access article distributed under the terms and conditions of the Creative Commons Attribution (CC BY) license (<https://creativecommons.org/licenses/by/4.0/>).

## 1. Introduction

Liquefied natural gas (LNG) is a clean energy source that is widely used in cryogenic engineering, industrial applications, power generation, and city gas distribution [1]. Traditional technologies for the liquefaction of natural gas include cascade liquefaction, mixed refrigerant liquefaction, and expansion liquefaction [2,3]. When compared with traditional natural gas liquefaction technologies, the recently developed supersonic liquefaction technology has several advantages, including minimal investment, a lower operational cost, a lighter structure, and easier operational methods [4,5]. Therefore, supersonic liquefaction technology has great application prospects.

As natural gas reaches a certain temperature and pressure, LNG may be obtained using a supersonic separator, which operates based on supersonic liquefaction technology [6]. The technology is based on the processes of condensation and cyclonic separation [7–9]. When saturated natural gas enters the Laval nozzle, the temperature of the gas decreases and its velocity becomes supersonic. As a result, condensed droplets are formed. The liquid droplets flowing through the cyclone separator are separated from the gas using a strong centrifugal force [10,11]. LNG is thus obtained.

The condensation process in the Laval nozzle plays an important role. A number of efforts have been made to investigate the supersonic condensation characteristics. The classical nucleation theory (CNT) model [12], internal consistent classical nucleation theory (ICCT) model [13], and improved ICCT model [14] have been carried out to predict the nucleation rate. In addition, many models, such as the Gyarmathy model [15] and Young model [16], have been used to describe the droplet growth process. The above-mentioned

models are beneficial to characterize the nucleation and growth processes. However, the effect of swirling flow on the condensation process was not considered.

With the advancement in computational fluid dynamics (CFD) simulations, numerous studies have been conducted using CFD technology with a condensation model to understand the characteristics of gas condensation in Laval nozzles. Ma et al. [17,18] established a turbulent Eulerian multifluid model to simulate supersonic gas flow in three dimensions and obtained the distribution of gas flow and condensation parameters. Cao and Yang [19] investigated the flowfield characteristics in a Laval nozzle under cyclonic flow conditions. They studied the effects of the nozzle structure and cyclonic intensity on the cooling and separation performance of the cyclone separator. Halama [20,21] used three Eulerian models to simulate a two-phase flow of steam through nonequilibrium condensation. Bian et al. [22] investigated the condensation of the  $\text{CH}_4\text{-CO}_2$  gas mixture in the supersonic nozzle. They studied the effects of the inlet  $\text{CO}_2$  fraction, inlet temperature, and inlet pressure on the flow and condensation parameters. Sun et al. [23] studied the homogeneous condensation process of sulfur dioxide on natural gas. Ding et al. [24] established a multiphase flow model considering droplet condensation and interphase forces to study the dewatering performance of supersonic separators. Shoghl et al. [25] used numerical methods to investigate the effects of structural and operational parameters on the separation efficiency of supersonic separators. In this study, the swirling flow on the separation of hydrocarbon droplets was considered.

Research on supersonic condensation characteristics is mainly studied under non-supersonic swirling flow conditions. In actual production, according to different working principles, supersonic separators can be divided into two categories. There is a supersonic separator whose cyclone section is installed behind the Laval nozzle, such as “Twister I” [26]. There is another supersonic separator whose cyclone section is installed in front of the Laval nozzle, such as “Twister II” [27]. For such devices, the effect of swirling flow on gas condensation should be considered. However, there is only a little literature on the liquefaction characteristics under swirling conditions. Therefore, this work discusses the effects of inlet pressure, inlet temperature, and export back pressure on the flow and condensation parameters. The key condensation parameters under supersonic swirling flow conditions were numerically calculated.

## 2. Physical Model

The supersonic separator comprises four components—the cyclone section, supersonic nozzle, straight pipe section, and diffuser section, as shown in Figure 1. The natural gas enters the supersonic nozzle tangentially. The high centrifugal force is generated by the cyclone section, which is a swirler with six vanes. The natural gas expands to supersonic velocities and liquid droplets are formed. Finally, the condensed droplets are removed from the dry gas by centrifugal force. Figure 1 presents the schematic of the supersonic separator along with the dimension of each of its parts. In the supersonic separator, the supersonic nozzle plays a vital role in gas condensation. The supersonic nozzle consists of four components: inlet stable section, subsonic contraction section, throat expansion section, and supersonic expansion section.

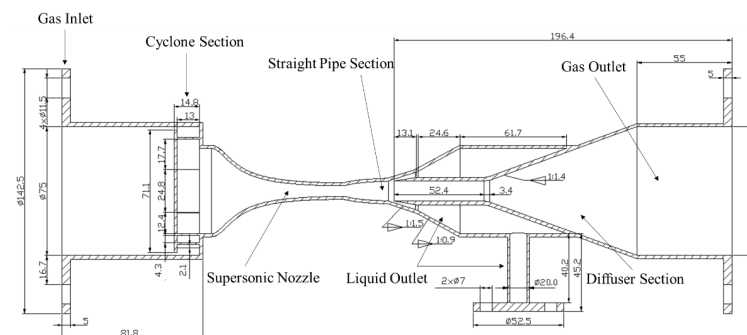


**Figure 1.** Schematic of the supersonic separator.

### 3. Simulation Methodology

#### 3.1. Governing Equations

It is assumed that the condensation nuclei are evenly distributed in the gas phase and that the collision probability is very small. Therefore, the collision between droplets is ignored in this study. The gas and liquid two-phase control equations of the supersonic condensate flow are established based on the Euler–Euler method [28].

The governing equations of the gas phase are as follows:

$$\frac{\partial \rho_g}{\partial t} + \frac{\partial}{\partial x_j} (\rho_g u_j) = S_m \quad (1)$$

$$\frac{\partial}{\partial t} (\rho_g u_i) + \frac{\partial}{\partial x_j} (\rho_g u_j u_i) = -\frac{\partial p}{\partial x_i} + \frac{\partial}{\partial x_j} \left[ u \left( \frac{\partial u_j}{\partial x_i} + \frac{\partial u_i}{\partial x_j} - \frac{2}{3} \delta_{ij} \frac{\partial u_j}{\partial x_j} \right) \right] + \frac{\partial}{\partial x_j} (-\rho_l \overline{u'_i u'_j}) + S_u \quad (2)$$

$$\frac{\partial}{\partial t} (\rho_g E) + \frac{\partial}{\partial x_j} (\rho_g u_j E + u_j p) = \frac{\partial}{\partial x_j} \left( k_{eff} \frac{\partial T}{\partial x_j} + u_i \tau_{eff} \right) + S_h \quad (3)$$

where  $t$  is the time,  $x$  is Cartesian coordinate,  $\rho_l$  is the liquid-phase density,  $\rho_g$  is the gas-phase density,  $p$  is the pressure,  $T$  is the temperature,  $u$  is the velocity,  $E$  is the total energy,  $\tau_{eff}$  is the effective stress tensor,  $k_{eff}$  is the effective thermal conductivity, and subscripts  $i$  and  $j$  represent  $x$  and  $y$ -axis, respectively.

The governing equations of the liquid phase are as follows:

$$\frac{\partial}{\partial t} (\rho Y_s) + \frac{\partial}{\partial x_j} (\rho u_j Y_s) = S_{Ys} \quad (4)$$

$$\frac{\partial \rho N_s}{\partial t} + \frac{\partial}{\partial x_j} (\rho N_s u_j) = J_s \quad (5)$$

$$r_d = \sqrt[3]{3Y_s / (4\pi\rho_l N_s)} \quad (6)$$

where  $\rho$  is the density,  $Y_s$  is the humidity,  $N_s$  is the droplet number,  $r_d$  is the droplet mean radius.  $S_m$ ,  $S_u$ ,  $S_h$ , and  $S_{Ys}$  are the source terms of mass, momentum, energy, and gas–liquid transport equations, as presented in Equations (7)–(10):

$$S_m = -m_s \quad (7)$$

$$S_u = -m_s u_i \quad (8)$$

$$S_h = m_s (h_{lg} - h) \quad (9)$$

$$S_{Ys} = m_s \quad (10)$$

where  $h$  is the vapor total enthalpy,  $h_{lg}$  is the latent heat of phase change, and  $m_s$  is the liquid mass per unit volume condensation in unit time, which may be derived as follows:

$$m_s = J_s \rho_l \frac{4\pi r_c^3}{3} + 4\pi r_d^2 N_s \rho_g \rho_l \frac{dr_d}{dt} \quad (11)$$

where  $r_c$  is the critical radius,  $J_s$  is the droplet nucleation rate, and  $\frac{dr_d}{dt}$  is the droplet growth rate.

#### 3.2. Condensation Model

The classical nucleation theory (CNT) model is employed to calculate the droplet nucleation rate, which is described as follows:

$$J_s(x) = \frac{\rho_g^2}{\rho_l} \sqrt{\frac{2\sigma}{\pi m_s}} \exp\left(\frac{16\pi\sigma^3}{3k\rho_l^2 R_g^2 T^3 \ln^2 S}\right) \quad (12)$$

$$\sigma = \left[ 1 - \frac{1}{3r \left( \frac{4}{3} \pi \frac{\rho_l}{m_s} \right)} \right] \sigma_\infty \quad (13)$$

$$\sigma_\infty = 0.2358(1 - T_r)^{1.256} [1 - 0.625(1 - T_r)] \quad (14)$$

where  $R_g$  is the gas constant,  $S$  is the degree of supersaturation,  $k$  is the Boltzmann constant,  $\sigma$  is the droplet surface tension,  $\sigma_\infty$  is the liquid plane surface tension.

In this work, the Gyarmathy model [23] is employed to calculate the droplet growth rate, which is derived as follows:

$$\frac{dr_d}{dt} = \frac{\lambda_g(1 - r_c/r)(T_s - T_g)}{\rho_l h_{lg} \left( r + \frac{\sqrt{8\pi}}{1.5 Pr_g} \frac{k}{k+1} \frac{2u\sqrt{RT_g}}{p_g} \right)} \quad (15)$$

$$r = \frac{2\sigma}{\rho_l R_g T_g \ln S} \quad (16)$$

where  $\lambda_g$  is the vapor-phase thermal conductivity,  $Pr_g$  is the vapor-phase Prandtl number,  $T_s$  is the droplet temperature,  $T_g$  is the gas-phase temperature, and  $P_g$  is the gas phase pressure.

### 3.3. Turbulence Model

In this work, the Reynolds stress model (RSM) was chosen as the turbulence model to present the characteristics of anisotropic turbulence. The RSM model has been reported to be an accurate model for defining highly anisotropic flows, such as the supersonic swirling flow [24]. The equations of the RSM model are not mentioned here for brevity but are well documented in other papers [29].

### 3.4. Real Gas Equation of State

Under the condition of low temperature and high pressure, the properties of gas deviate from those of ideal gas. Therefore, the real gas equation of state should be used. In this study, the BWRS equation [30] was selected for calculating the properties of natural gas. The mole composition of natural gas is as follows: 90.8% CH<sub>4</sub>, 7.1% C<sub>2</sub>H<sub>6</sub>, 0.1% C<sub>3</sub>H<sub>8</sub>.

## 4. Numerical Illustration

The simulations in this study for the two-phase flow of steam in the supersonic separator were performed using the ANSYS Workbench 16.0 (ANSYS, Canonsburg, PA, USA) software package. The calculation flow of the simulation model is shown in Figure 2. User-defined scalar (UDS) flux functions were used to establish the governing equations of the liquid phase. User-defined functions (UDFs) were used to add the source terms caused by condensation to the governing equations.

The SIMPLE algorithm [31] was adopted for the coupling of the velocity and pressure fields. The governing equations of gas-liquid flow, turbulent kinetic energy equation, and dissipation rate equation were discretized by a second-order upwind scheme [6]. The pressure was employed at the inlet and outlet boundary surfaces. The specified pressure, total temperature, turbulence parameters, and gas mole fraction should be fixed for the inlet pressure. No-slip and adiabatic boundary conditions [32] were applied to the walls. In this study, a convergence criterion of  $10^{-5}$  was assigned for all the equations, and the relative error of the inlet and outlet mass flows was maintained below 1%. The specific settings for the numerical simulation are shown in Table 1.

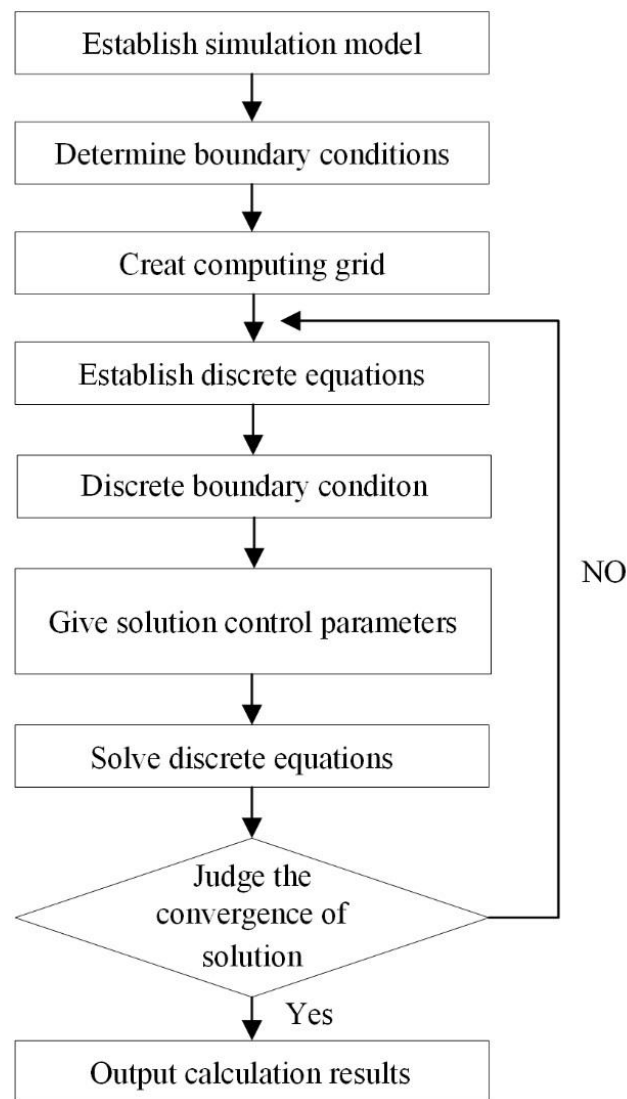


**Figure 2.** Flow chart of the calculation of simulation model.

**Table 1.** Numerical schemes for this simulation.

| Items                      | Settings  |
|----------------------------|---|
| Computational platform     | ANSYS Workbench 16.0  |
| Solver type                | Density-Based   |
| Algorithm                  | SIMPLE algorithm  |
| Discretization             | Second-order upwind scheme  |
| Inlet boundary conditions  | Pressure inlet with specified pressure, total temperature, turbulence parameters, and gas mole fraction |
| Outlet boundary conditions | Pressure outlet   |
| Wall boundary conditions   | No-slip and adiabatic   |
| Convergence criterion      | $10^{-5}$   |

As the flow and geometry of the supersonic separator were complex, three unstructured meshes with grid densities of 35,000, 70,241, and 100,000, respectively, were used to account for the mesh independence of the supersonic separator. The variation in the liquid generation rate with different cell numbers is shown in Figure 3 (the inlet pressure and the outlet pressure are 2 MPa and 0.4 MPa, respectively). The simulation results showed that the mesh with a grid density of 70,241 was the optimal one in terms of accuracy and computational cost. This mesh was used for all simulations. The three-dimensional grid system of the supersonic separator is shown in Figure 4.

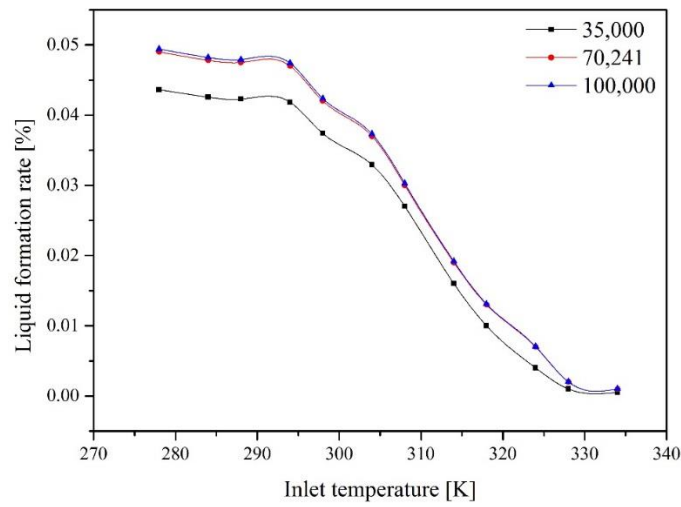


Figure 3. Simulation results of liquid generation rate corresponding to different cells.

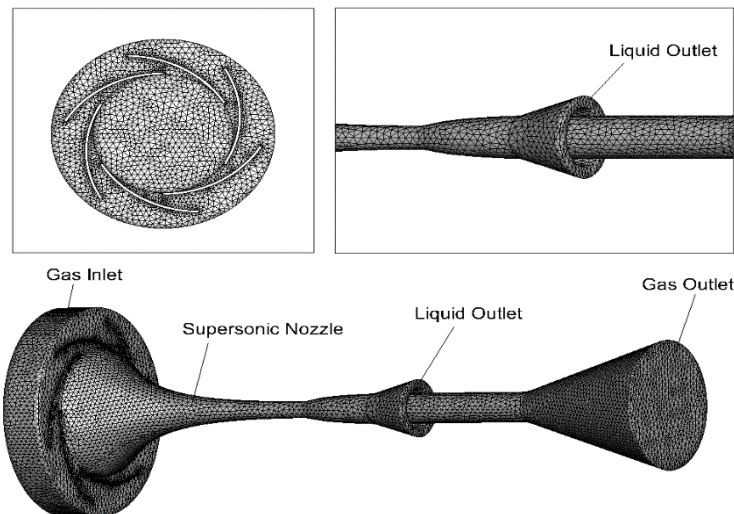


Figure 4. Three-dimensional grid of supersonic separator.

### 5. Model Verification

An experimental system was set up to study the supersonic condensation characteristics; the flowchart of the supersonic condensation process and experimental flow system is shown in Figure 5. The dimensions of the experimental nozzle are shown in Figure 1.

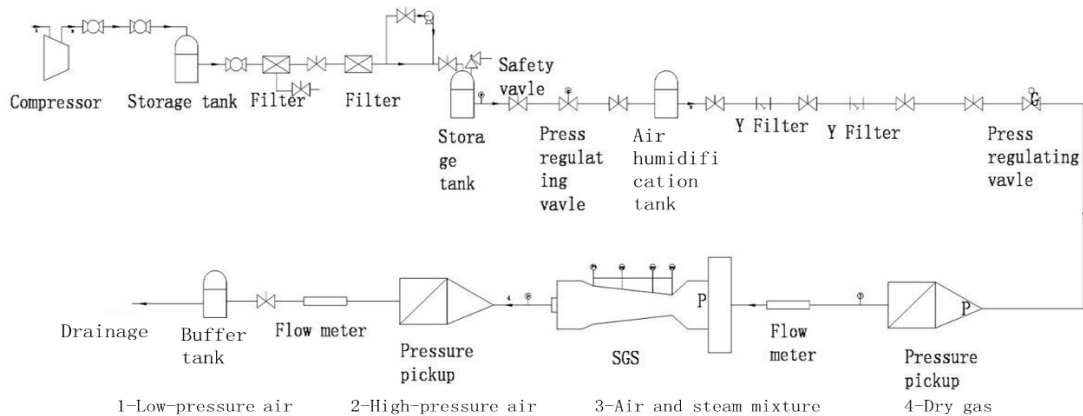
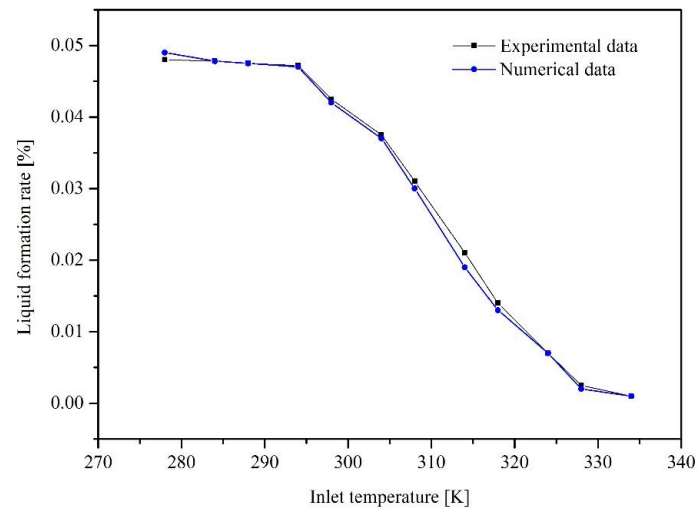
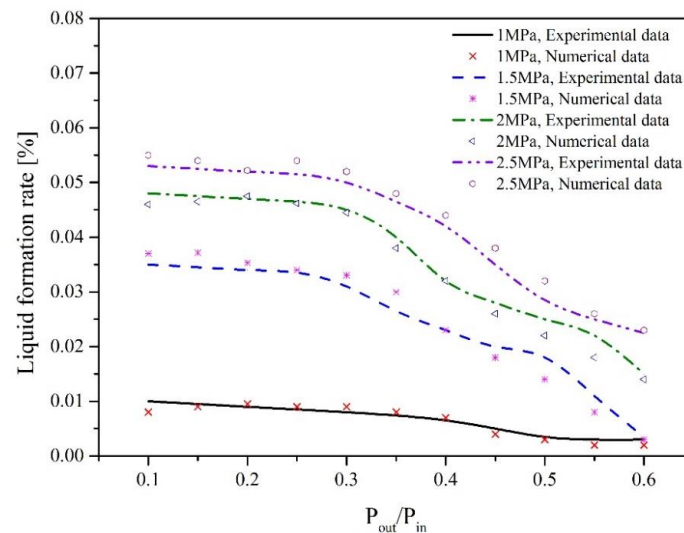


Figure 5. Flowchart of the supersonic condensation process and experimental flow system.

Figure 6 shows the experimental and simulation data of the variation in the liquid generation rate with the change in inlet temperature when the inlet pressure was 2 MPa and outlet pressure was 0.4 MPa. Figure 7 illustrates the comparison results between the experimental and simulation data of the variation in the liquid generation rate with the change in inlet pressure and back pressure. The experimental conditions were as follows: the inlet temperature was kept at 288 K, and the inlet pressure was 1 MPa, 1.5 MPa, 2 MPa, and 2.5 MPa, respectively. The ratio of export back pressure to inlet pressure varied from 0.1 to 0.6. It can be seen from Figures 6 and 7 that the numerical results agree with the experimental results well, and the prediction error of the theoretical model is less than 10%.



**Figure 6.** Variation in the liquid formation rate with the change in inlet temperature.



**Figure 7.** Variation in the liquid formation rate with the change in inlet pressure and back pressure.

## 6. Results and Discussion

### 6.1. Effect of Export Back Pressure on the Condensation Parameters

The effect of export back pressure on the condensation parameters was calculated numerically. The distribution pattern of the condensation parameters in the supersonic separator for different export back pressure values was obtained by keeping the inlet pressure at 4 MPa and inlet temperature at 240 K.

The Mach number distribution along the axial cross-section of the supersonic separator is shown in Figure 8. When the export back pressure was increased from 1.6 to 2.2 MPa, the maximum Mach number decreased from 1.72 to 1.64. The maximum Mach number in

this range of export back pressure was found to be mainly distributed in the straight pipe section. As only a very small number of liquid droplets were able to be obtained at the separation gap, the liquefaction of natural gas was almost unattainable. When the export back pressure was increased to 2.3 MPa, the maximum Mach number further decreased to 1.59, and the position of the maximum Mach number was found to move toward the inlet of the straight pipe section beyond the separation gap. As a result, a large number of liquid droplets could be effectively separated out from the separation gap by the cyclone separator. When the export back pressure was further increased to 2.4 MPa, the distribution of the maximum Mach number was found to have entered the expansion section of the supersonic nozzle, which was expected to lead to premature condensation of the liquid and low liquefaction efficiency. It can be seen that the export back pressure at this point is neither as low as possible nor as high as possible and that there is an optimal range of export back pressure. One of the bases for determining the optimal range is that the maximum Mach number region in the device should be at the inlet of the straight pipe section beyond the separation gap. In this work, the optimal export back pressure was found to be 2.3 MPa.

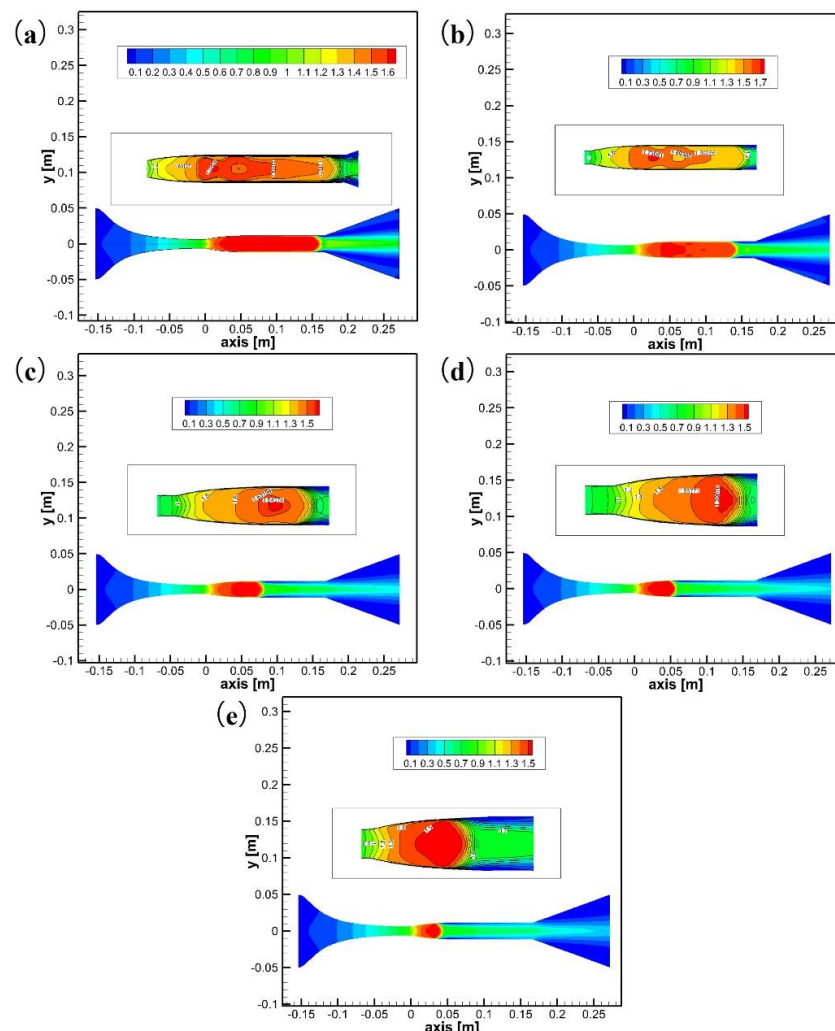


**Figure 8.** Mach number distribution along the axial cross-section of the supersonic separator at export back pressure values (a) 1.6 MPa; (b) 1.8 MPa; (c) 2.2 MPa; (d) 2.3 MPa, and (e) 2.4 MPa.

The simulation results of the nucleation rates in the supersonic separator are shown in Figure 9. The change in the export back pressure has only a minor effect on the nucleation rates. However, the length of the condensation nucleation zone is affected significantly due to the variation in the export back pressure. It may be observed that the condensation

nucleation region is the longest when the export back pressure is 1.8 MPa. However, the length of the condensation nucleation zone remains almost the same even when the pressure is varied from 2.2 to 2.4 MPa. In addition, in this pressure range, the formation of the condensation nucleation zone is in the supersonic nozzle expansion section between the exit and the inlet of the straight pipe section. Therefore, when the effect of the export back pressure on the distribution of the nucleation rate is considered, the first step is to determine whether the condensation nucleation region is in the region where effective separation can be achieved.

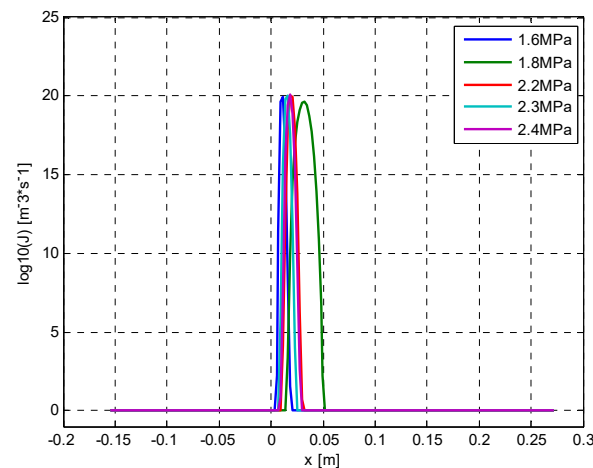


**Figure 9.** Nucleation rate curves along the axial cross-section of the supersonic separator.

Figure 10 illustrates the humidity distribution curves along the axial cross-section of the supersonic separator. The humidity inside the device increases with the increase in the export back pressure. The observation is evident for the increase in the export back pressure from 1.6 to 2.3 MPa. However, when the export back pressure becomes 2.4 MPa, the humidity inside the device starts decreasing. This is mainly because the static pressure in the device increases with the increase in the back pressure. The gas viscosity increases with the increase in the pressure. In addition, the increased heat generated due to the friction between molecules vaporizes part of the condensation core. It can be seen that there is an optimal range of export back pressure. The maximum humidity distribution regions under different export back pressure conditions are shown in Figure 11. As seen in the figure, with the increase in the back pressure, the maximum humidity distribution area gradually moves from the straight pipe section to the nozzle expansion section. When the value of export back pressure reaches 2.3 MPa, the maximum humidity distribution region is located between the nozzle expansion section and the straight section of the entrance. In this case, the droplets can flow out of the separation gap due to the swirling flow.

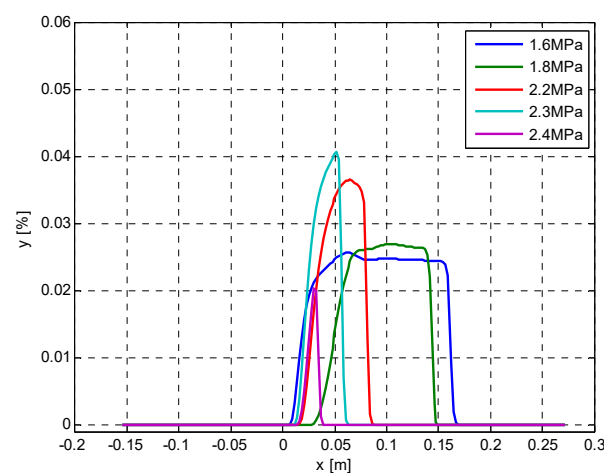


**Figure 10.** Humidity distribution curves along the axial cross-section of the supersonic separator.

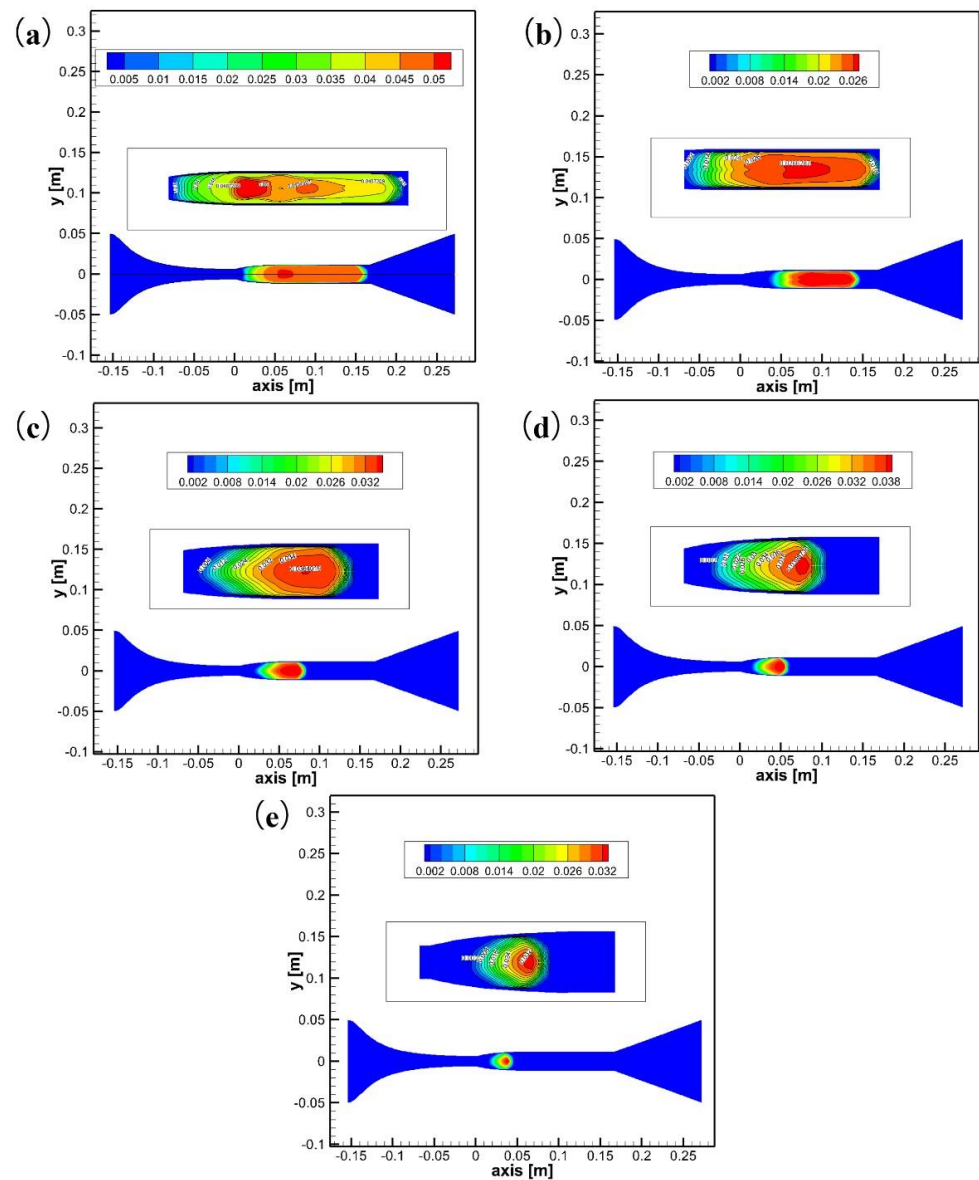


**Figure 11.** Humidity distribution along the axial cross-section of the supersonic separator at export back pressure values (a) 1.6 MPa; (b) 1.8 MPa; (c) 2.2 MPa; (d) 2.3 MPa, and (e) 2.4 MPa.

### 6.2. Effect of Inlet Temperature on the Condensation Parameters

The effects of inlet temperature on the condensation parameters are numerically at the inlet pressure of 4 MPa and the export back pressure of 2.3 MPa. The Mach number distribution along the axial cross-section of the supersonic separator under different inlet temperature conditions are shown in Figure 12. The figure indicates that the Mach number distribution is consistent in the supersonic separator for different inlet temperatures, which demonstrates that the change range of heat ratio is small in the investigated temperature range.

Figure 13 shows the nucleation rate curves along the axial cross-section of the supersonic separator for inlet temperatures 220, 230, 240, 250, 260, 265, and 270 K. It can be observed that, as the temperature decreases, the location of gas condensation nucleation moves toward the expansion section of the nozzle and the distribution interval becomes narrower. Increasing the inlet temperature leads to a decrease in the rate of subcooling. Spontaneous condensation occurs at a delayed time and further away from the nozzle expansion section, which is not conducive to gas liquefaction. In addition, it can be seen in Figure 13 that the nucleation rates are consistent when the temperature is between 220 and 250 K.

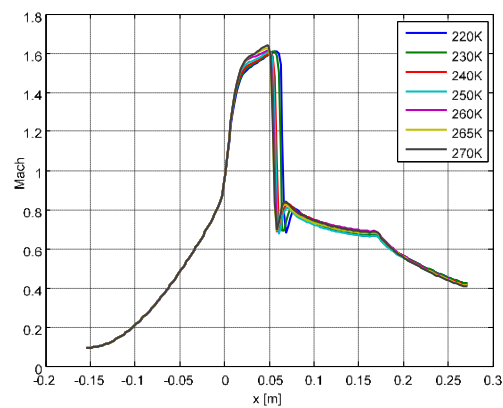


**Figure 12.** Mach number distribution curves along the axial cross-section of the supersonic separator at temperatures 220, 230, 240, 250, 260, 265, and 270 K.

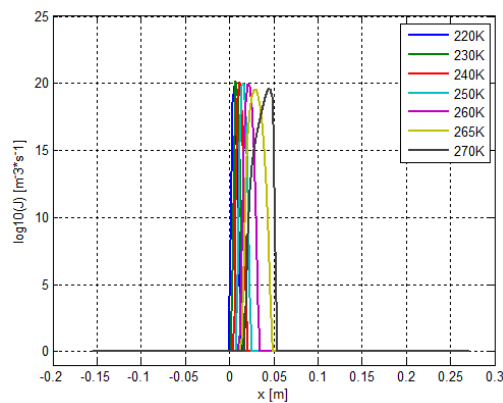


**Figure 13.** Nucleation rate curves along the axial cross-section of the supersonic separator at temperatures 220, 230, 240, 250, 260, 265, and 270 K.

Figure 14 shows the humidity distribution curves along the axial cross-section of the supersonic separator for inlet temperatures 220, 230, 240, 250, 260, 265, and 270 K. Humidity decreases with the increase in temperature. However, there is not much difference in the humidity for temperatures between 220 and 250 K. It can be seen that the humidity decreases rapidly when the temperature rises to 260 K. Therefore, there is an optimal range of inlet temperature. Considering the energy consumption of the system, a higher temperature should be selected as the inlet temperature in the optimal interval. In this study, 240 K was chosen as the optimal inlet temperature. If 250 K is to be considered as the inlet temperature, it is possible that a slight increase in the temperature will lead to a rapid decrease in humidity in the event of production fluctuations.

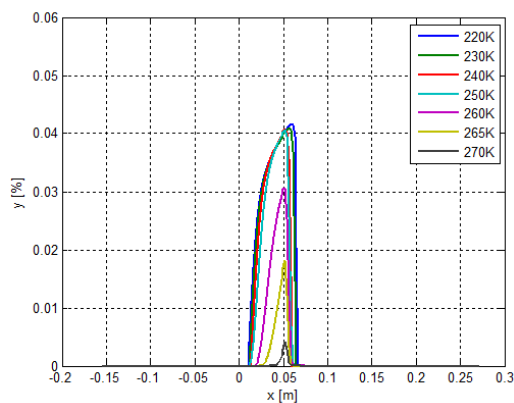


**Figure 14.** Humidity distribution curves along the axial cross-section of the supersonic separator at temperatures 220, 230, 240, 250, 260, 265, and 270 K.

### 6.3. Effect of Inlet Pressure on the Condensation Parameters

The effect of inlet pressure on the condensation parameters is numerically calculated, keeping the pressure ratio at 0.575 and inlet temperature at 240 K. The Mach number distribution curves along the axial cross-section of the supersonic separator under different inlet pressure conditions are shown in Figure 15. It can be observed that an increase in the inlet pressure has a lesser effect on the location of the surge generation and a higher effect on the Mach number, which is in accordance with the basic principles of gas dynamics.

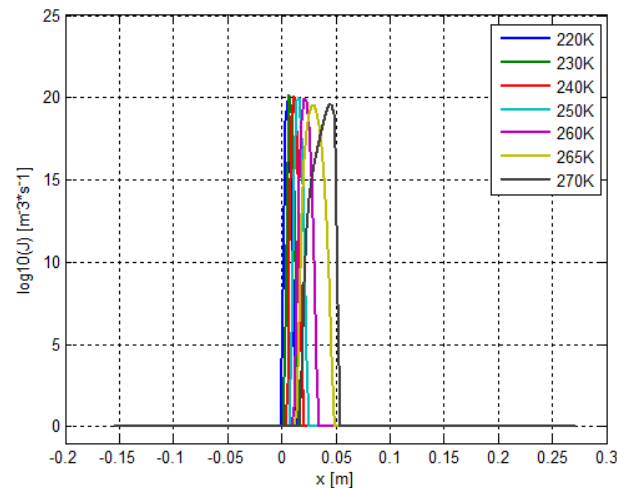


**Figure 15.** Mach number distribution curves along the axial cross-section of the supersonic separator at inlet pressure values 2, 3.5, 4, 5, and 5.5 MPa.

Figure 16 shows the nucleation rate curves along the axial cross-section of the supersonic separator for inlet pressures 2, 3.5, 4, 5, and 5.5 MPa. The maximum nucleation rate decreases with the increase in the inlet pressure. In addition, it was observed that the position of condensation appears earlier with the increase in the inlet pressure.

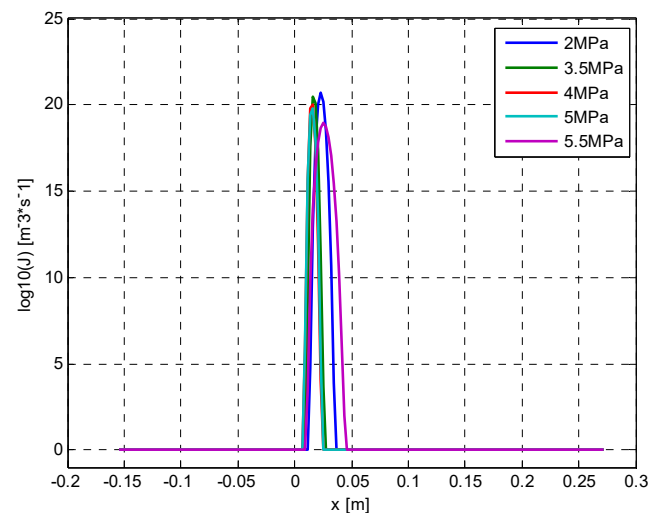


**Figure 16.** Nucleation rate curves along the axial cross-section of the supersonic separator at inlet pressure values 2, 3.5, 4, 5, and 5.5 MPa.

Figure 17 shows the humidity distribution curves along the axial section of the supersonic separator for inlet pressure values of 2, 3.5, 4, 5, and 5.5 MPa. When the inlet pressure is between 2 and 5 MPa, both humidity and its distribution area increase with the increase in the pressure value. However, when the inlet pressure is 5.5 MPa, the humidity decreases rapidly. As the inlet pressure increases, the humidity distribution area will extend into the straight pipe section, resulting in some droplets not being separated out effectively and vaporized again during the flow into the straight pipe section. It can be seen that the inlet

pressure of 5 MPa is the inflection point for humidity reduction and the inlet pressure of 4 MPa is the optimal value.

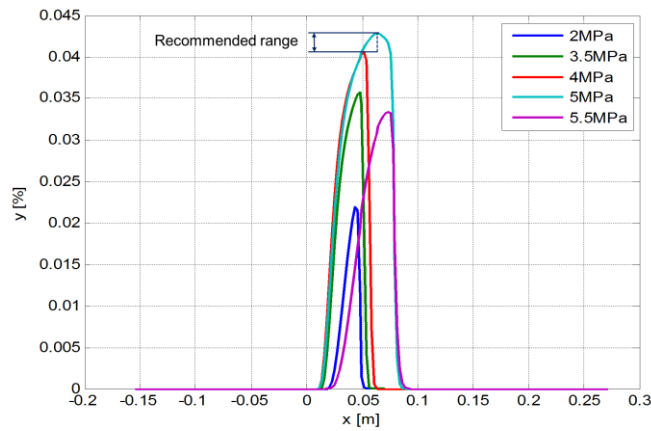


**Figure 17.** Humidity distribution curves along the axial cross-section of the supersonic separator at internal pressure values 2, 3.5, 4, 5, and 5.5 MPa.

6.4. Liquefaction Performance of Three-Dimensional Full Flowfield Simulation Device

Based on the above analysis, for a supersonic separator (see Figure 1) with an identified size and processing capacity, the optimum operating parameters were found to be as follows: inlet pressure, 4 MPa; inlet temperature, 240 K, and export back pressure, 2.3 MPa. Figures 18 and 19 show the Mach number and humidity distribution inside the supersonic cyclonic separation device at the optimal parameter conditions, respectively.

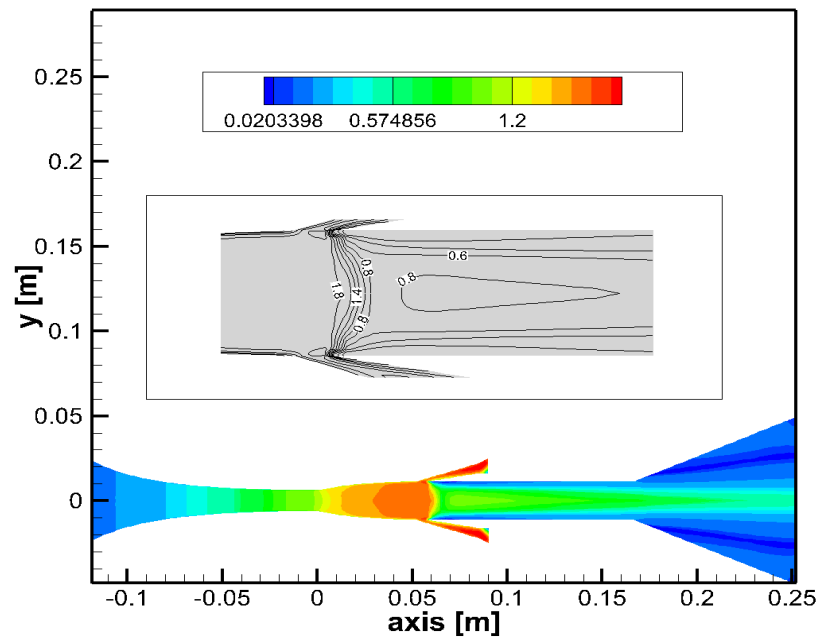


**Figure 18.** Internal Mach number distribution along the axial cross-section of the supersonic separator.

Figure 18 presents Mach number distribution along the axial cross-section of the supersonic separator under the optimal parameter conditions. The excitation wave is generated just to the right of the separation gap, at the entrance of the straight pipe section. Figure 19 shows that the separation gap has a high humidity distribution and harvests the droplets well. The flow characteristics of the device under three-dimensional, full-scale simulation with spin flow illustrate that the selected operating parameters are reasonable.

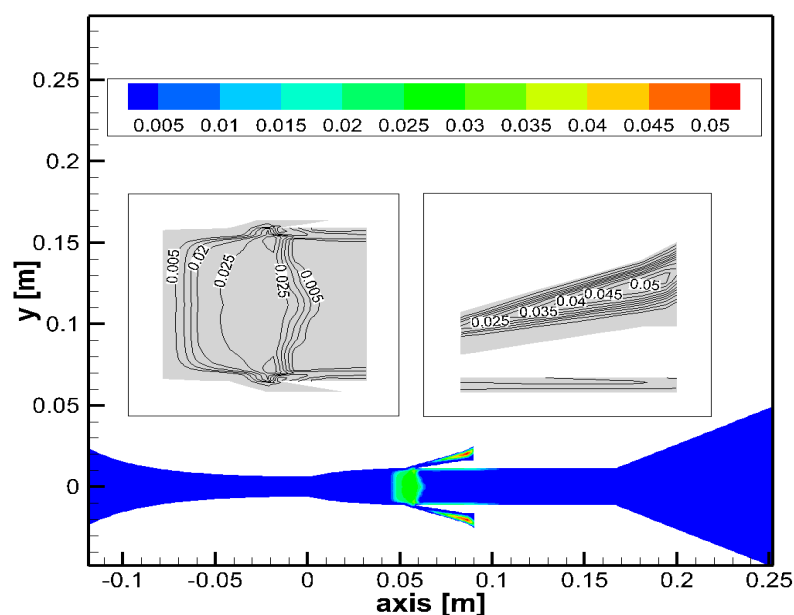


Figure 19. Humidity distribution along the axial cross-section of the supersonic separator.

## 7. Conclusions

To study the condensation process in a supersonic separator, a mathematical model for the supersonic condensate flow of natural gas was given out. Experimental results demonstrate that the model has good results with a prediction error of less than 10%. The effects of export back pressure, inlet temperature, and inlet pressure on the condensation parameters were investigated. Based on our study, the following conclusions were drawn. It is important to identify the optimal value of export back pressure. The export back pressure in the optimal range can make the extreme Mach number region in the device to be at the inlet of the straight pipe section after the separation gap. The condensation nucleation pole area and the maximum humidity distribution area should be between the nozzle expansion section and the inlet of the straight pipe section.

Variations in the inlet temperature were found to have only a small effect on the Mach number and the location of the surge generation. With the decrease in the inlet temperature, the condensation position moved forward. Continuing to lower the temperature beyond a certain level did not significantly increase the humidity. Therefore, it is important to select a higher temperature as the inlet temperature in the optimal interval to reduce the energy consumption of the system.

With the increase in the inlet pressure, the condensation position moves forward. The set inlet pressure should not be higher than the pressure corresponding to the humidity inflection point value. At this pressure, the humidity distribution area should be behind the supersonic nozzle expansion section and before the inlet of the straight pipe section to ensure the maximum liquefaction rate and best separation efficiency.

**Author Contributions:** X.L. conceived and designed the study, conducted experiments and software simulations, and wrote the original draft. Q.H. was responsible for supervision, validation, reviewing, and editing. Y.T. and L.M. are responsible for conducting experiments and numerical simulations. All authors have read and agreed to the published version of the manuscript.

**Funding:** This research was supported by the National Natural Science Foundation of China (No. 51904051), the Natural Science Foundation of Chongqing, China (No. cstc2019jcyj-msxmX0745), and the Science and Technology Research Program of the Chongqing Municipal Education Commission (Nos. KJQN201801512 and KJZD-K201901505).

**Data Availability Statement:** Not applicable.

**Conflicts of Interest:** The authors declare no conflict of interest.

## Nomenclature

|                 |                                       |   |
|-----------------|---------------------------------------|---|
| $dr/dt$         | [-]                                   | droplet growth rate                                   |
| $E$             | [J kg <sup>-1</sup> ]                 | total energy  |
| $h$             | [J kg <sup>-1</sup> ]                 | vapor total enthalpy                                  |
| $h_{lg}$        | [J kg <sup>-1</sup> ]                 | latent heat of phase change                           |
| $J_s$           | [m <sup>-3</sup> s <sup>-1</sup> ]    | droplet nucleation rate                               |
| $k$             | [-]                                   | Boltzmann constant                                    |
| $k_{eff}$       | [W m <sup>-1</sup> K <sup>-1</sup> ]  | effective thermal conductivity                        |
| $m_s$           | [kg m <sup>-3</sup> s <sup>-1</sup> ] | liquid mass per unit volume condensation in unit time |
| $N_s$           | [kg <sup>-1</sup> ]                   | droplet number  |
| $p$             | [Pa]                                  | pressure  |
| $P_g$           | [Pa]                                  | gas-phase pressure                                    |
| $P_{rg}$        | [-]                                   | vapor-phase Prandtl number                            |
| $R_g$           | [-]                                   | gas constant  |
| $r_c$           | [m]                                   | critical radius                                       |
| $r_d$           | [m]                                   | droplet mean radius                                   |
| $S$             | [-]                                   | degree of supersaturation                             |
| $S_m$           | [kg m <sup>-3</sup> s <sup>-1</sup> ] | source term of mass                                   |
| $S_u$           | [kg m <sup>-2</sup> s <sup>-2</sup> ] | source term of momentum                               |
| $S_h$           | [J m <sup>-3</sup> s <sup>-1</sup> ]  | source term of energy                                 |
| $S_{\gamma S}$  | [kg m <sup>-3</sup> s <sup>-1</sup> ] | source terms of gas–liquid transport equations        |
| $T$             | [K]                                   | temperature   |
| $T_s$           | [K]                                   | droplet temperature                                   |
| $T_g$           | [K]                                   | gas-phase temperature                                 |
| $t$             | [s]                                   | time  |
| $u$             | [m s <sup>-1</sup> ]                  | velocity  |
| $x$             | [-]                                   | Cartesian coordinate                                  |
| Greek symbols   |                                       |   |
| $\lambda_g$     | [W m <sup>-1</sup> K <sup>-1</sup> ]  | vapor-phase thermal conductivity                      |
| $\rho$          | [kg m <sup>-3</sup> ]                 | density   |
| $\rho_l$        | [kg m <sup>-3</sup> ]                 | liquid-phase density                                  |
| $\rho_g$        | [kg m <sup>-3</sup> ]                 | gas-phase density                                     |
| $\sigma$        | [N m <sup>-1</sup> ]                  | droplet surface tension                               |
| $\sigma_\infty$ | [N m <sup>-1</sup> ]                  | liquid plane surface tension                          |
| $\tau_{eff}$    | [-]                                   | effective stress tensor                               |

## References

1. Sakmar, S.L. *Energy for the 21st Century: Opportunities and Challenges for Liquefied Natural Gas (LNG)*; Edward Elgar Publishing: Cheltenham, UK, 2013.
2. Kumar, S.; Kwon, H.-T.; Choi, K.-H.; Cho, J.H.; Lim, W.; Moon, I. Current status and future projections of LNG demand and supplies: A global prospective. *Energy Policy* **2011**, *39*, 4097–4104. [[CrossRef](#)]
3. Zhang, G.; Zheng, J.; Yang, Y.; Liu, W. A novel LNG cryogenic energy utilization method for inlet air cooling to improve the performance of combined cycle. *Appl. Energy* **2016**, *179*, 638–649. [[CrossRef](#)]
4. He, T.; Ju, Y. Design and optimization of natural gas liquefaction process by utilizing gas pipeline pressure energy. *Appl. Therm. Eng.* **2013**, *57*, 1–6. [[CrossRef](#)]
5. Interlenghi, S.F.; de Medeiros, J.L.; Ofélia de Queiroz, F.A. On small-scale liquefaction of natural gas with supersonic separator: Energy and second law analyses. *Energy Convers. Manag.* **2020**, *221*, 113117. [[CrossRef](#)]
6. Bian, J.; Cao, X.; Yang, W.; Song, X.; Xiang, C.; Gao, S. Condensation characteristics of natural gas in the supersonic liquefaction process. *Energy* **2019**, *168*, 99–110. [[CrossRef](#)]
7. Mokhatab, S.; Poe, W.A. *Handbook of Natural Gas Transmission and Processing*; Gulf Professional Publishing: Houston, TX, USA, 2012.
8. Faiz, R.; Al-Marzouqi, M. Insights on natural gas purification: Simultaneous absorption of CO<sub>2</sub> and H<sub>2</sub>S using membrane contactors. *Sep. Purif. Technol.* **2011**, *76*, 351–361. [[CrossRef](#)]
9. Shooshtari, S.R.; Shahsavand, A. Reliable prediction of condensation rates for purification of natural gas via supersonic separators. *Sep. Purif. Technol.* **2013**, *116*, 458–470. [[CrossRef](#)]
10. Bian, J.; Cao, X.; Yang, W.; Gao, S.; Xiang, C. A new liquefaction method for natural gas by utilizing cold energy and separating power of swirl nozzle. *AIChE J.* **2020**, *66*, e16811. [[CrossRef](#)]

11. Haghghi, M.; Hawboldt, K.A.; Abdi, M.A. Supersonic gas separators: Review of latest developments. *J. Nat. Gas. Sci. Eng.* **2015**, *27*, 109–121. [[CrossRef](#)]
12. Guo, D.; Cao, X.; Ding, G.; Zhang, P.; Liu, Y.; Bian, J. Crystallization and nucleation mechanism of heavy hydrocarbons in natural gas. *Energy* **2022**, *239*, 122071. [[CrossRef](#)]
13. Girshick, S.L. Comment on: "Self-consistency correction to homogeneous nucleation theory". *J. Chem. Phys.* **1991**, *94*, 826–827. [[CrossRef](#)]
14. Lamanna, G. *On Nucleation and Droplet Growth in Condensing Nozzle Flows*; Eindhoven University of Technology: Eindhoven, The Netherlands, 2002.
15. Gyarmathy, G. The spherical droplet in gaseous carrier streams: Review and synthesis. *Multiph. Sci. Technol.* **1982**, *1*, 99–279. [[CrossRef](#)]
16. Young, J. The condensation and evaporation of liquid droplets at arbitrary Knudsen number in the presence of an inert gas. *Int. J. Heat Mass Transf.* **1993**, *36*, 2941–2956. [[CrossRef](#)]
17. Qingfen, M.; Dapeng, H.; Gaohong, H.; Shijun, H.; Wenwei, L.; Qiaolian, X.; Yuxin, W. Performance of inner-core supersonic gas separation device with droplet enlargement method. *Chin. J. Chem. Eng.* **2009**, *17*, 925–933.
18. Ma, Q.-F.; Hu, D.-P.; Jiang, J.-Z.; Qiu, Z.-H. Numerical study of the spontaneous nucleation of self-rotational moist gas in a converging–diverging nozzle. *Int. J. Comput. Fluid Dyn.* **2010**, *24*, 29–36. [[CrossRef](#)]
19. Cao, X.; Yang, W. Numerical simulation of binary-gas condensation characteristics in supersonic nozzles. *J. Nat. Gas Sci. Eng.* **2015**, *25*, 197–206. [[CrossRef](#)]
20. Halama, J.; Hric, V. Numerical solution of steam flow in a nozzle using different non-equilibrium condensation models. *Appl. Math. Comput.* **2016**, *272*, 657–669. [[CrossRef](#)]
21. Halama, J.; Fořt, J. Numerical simulation of transonic flow of wet steam in nozzles and turbines. *Computing* **2013**, *95*, 303–318. [[CrossRef](#)]
22. Bian, J.; Jiang, W.; Hou, D.; Liu, Y.; Yang, J. Condensation characteristics of CH<sub>4</sub>-CO<sub>2</sub> mixture gas in a supersonic nozzle. *Powder Technol.* **2018**, *329*, 1–11. [[CrossRef](#)]
23. Sun, W.; Cao, X.; Yang, W.; Zhao, X. CFD modeling on non-equilibrium condensation process of H<sub>2</sub>S in CH<sub>4</sub>-H<sub>2</sub>S mixture expansion through supersonic nozzles. *Fuel. Process. Technol.* **2018**, *170*, 53–63. [[CrossRef](#)]
24. Ding, H.; Sun, C.; Wang, C.; Wen, C.; Tian, Y. Prediction of dehydration performance of supersonic separator based on a multi-fluid model with heterogeneous condensation. *Appl. Therm. Eng.* **2020**, *171*, 115074. [[CrossRef](#)]
25. Shoghl, S.N.; Naderifar, A.; Farhadi, F.; Pazuki, G. A novel strategy for comprehensive optimization of structural and operational parameters in a supersonic separator using computational fluid dynamics modeling. *Sci. Rep.* **2021**, *11*, 21850. [[CrossRef](#)] [[PubMed](#)]
26. Okimoto, D. Supersonic gas conditioning. *World Oil* **2002**, *8*, 89–91.
27. Schinkelshoek, P.; Epsom, H. Supersonic gas conditioning-low pressure drop twister for NGL recovery. In Proceedings of the Offshore Technology Conference, Houston, TX, USA, 1–4 May 2006; OnePetro: Richardson, TX, USA, 2006.
28. Bian, J.; Cao, X.; Yang, W.; Guo, D.; Xiang, C. Prediction of supersonic condensation process of methane gas considering real gas effects. *Appl. Therm. Eng.* **2020**, *164*, 114508. [[CrossRef](#)]
29. Hu, L.Y.; Zhou, L.X.; Zhang, J.; Shi, M. Studies on strongly swirling flows in the full space of a volute cyclone separator. *AIChE J.* **2005**, *51*, 740–749. [[CrossRef](#)]
30. Starling, K.E.; Han, M. Thermo data refined for LPG–14. *Mixtures. Hydrocarb. Process.* **1972**, *51*, 129–132.
31. Yang, Y.; Walther, J.H.; Yan, Y.; Wen, C. CFD modeling of condensation process of water vapor in supersonic flows. *Appl. Therm. Eng.* **2017**, *115*, 1357–1362. [[CrossRef](#)]
32. Bian, J.; Cao, X.; Yang, W.; Edem, M.A.; Yin, P.; Jiang, W. Supersonic liquefaction properties of natural gas in the Laval nozzle. *Energy* **2018**, *159*, 706–715. [[CrossRef](#)]